Chapter 28 – NUMERICAL SOLUTIONS FOR THE VFE-2 CONFIGURATION ON STRUCTURED GRIDS

by

Emre Gurdamar, Yüksel Ortakaya,
Serpil Kaya, Bulent Korkem

To understand and model vortical flows, experimental investigations and flow simulations were carried out within the task group of NATO RTO AVT-113 International Vortex Flow Experiment. As being a member of the task group, TAI performed flow simulations on structured grids with an in-house, three dimensional Navier-Stokes solver, xFLOWg. Aim is to understand the physical characteristics of the vortical flow on delta wing configurations and to realize the ability of the flow solver for complex flow simulations.

TAI has studied a number of subsonic and transonic test cases in VFE-2 facet of AVT-113 RTO Applied Vehicles Technology panel. These test cases were medium radius and sharp leading edge delta wing configurations. In the early stages of the study, TAI carried out computations for 20 test cases (Table 28-1) to identify distinct flow characteristics. Another idea behind choosing such a test matrix was to provide detailed information about the capabilities of the numerical approaches and the flow solver used.

Reynolds-Averaged Navier-Stokes simulations were performed for the chosen 20 test cases. The simulations were carried out with algebraic Baldwin-Lomax turbulence model. Based on the first results, it is seen that essential features of the flows were not resolved accurately. Pressure peaks, representing the vortical region, did not match well with the experimental data. Since turbulence plays an important role for vortex dominated flows, it is decided to add a new turbulence model to xFLOWg. Based on this fact, one-equation Spalart-Allmaras turbulence model which is widely known and used especially for external aerodynamics, has been implemented for better vortical flow resolution. In addition to 4 cases selected from the first 20 cases studied, two cases at higher angle of attack were chosen to compare the turbulence models and see the effects on the flow field. They were listed in Table 28-5. It was assumed that flow is fully turbulent. Noteworthy improvement in the results has been achieved. Once accurate results were obtained, test matrix was limited to nine cases to concentrate on the physics of the flow for the identified flow regimes (Table 28-2, Table 28-3, Table 28-4).

Experiments showed that distinct flow regimes can be classified with respect to angle of attack. Special attention was paid on the separated vortical flow without vortex breakdown at angles of attack smaller than 20 degrees. Flow is attached and vortex formation is not observed at angles smaller than 4 degrees, therefore there was no interest to low angles of attack cases. Larger than 20 degrees, vortex breakdown phenomenon is present in the flow field. For transonic cases, another challenge was to resolve the shock-vortex interaction accurately. Implementation of Spalart-Allmaras turbulence model provided better simulation capability such that those distinct regions could be captured.

The common structured grid provided by EADS-M was used for all the simulations. Results showed that besides the turbulence model, grid must also be investigated to resolve some of the characteristics of the flow field. The suction peaks on the upper surface of the wing were poorly matched with the experimental data. Some computations were performed regarding this issue but more consideration is necessary, and therefore, they are not presented here. One outlook might be to make a grid dependency study, another would be to make solution based mesh adaptation study and see the effects on the results.

To analyse the flow simulation results, detailed pressure distribution at a variety of chord wise locations were compared with the measurements. These plots were useful to clarify onset of separation for blunt leading edge configuration. For better understanding of the flow features and comparison, vorticity lines were also drawn. Special interest was given to the cases (Table 28-2, Table 28-3, Table 28-4) in order to show the influence of compressibility, angle of attack and leading edge bluntness on the flow field.

In conclusion, numerical simulations provided clear pictures for the flow field. Even though the geometry is simple, governed flow phenomena is quite complex and it is shown that the complex flow features can be simulated with a suitable Navier-Stokes solver and turbulence model. This flow simulation capability is crucial for understanding the details of flow field and effective wind tunnel testing.

28.1 COMPUTATIONAL DETAILS

28.1.1 Flow Solver

xFLOWg is a parallel, three dimensional, structured, multi-block, finite-volume, Reynolds-Averaged Navier-Stokes solver developed at TAI [[28-1], [28-2], [28-3], [28-4]]. Steady or unsteady flows can be simulated with xFLOWg. Fifth order accurate WENO and first, second and third order accurate Roe scheme with MUSCL have been implemented for inviscid flux calculations. For viscous flux calculations, second order accurate central difference scheme has been used. Multi-stage Runge-Kutta or LU-SGS scheme can be used for time integration. It contains Baldwin-Lomax, Spalart Allmaras turbulence models. Additionally, standard k-omega, and SST k-omega turbulence models have been implemented.

In the studies, steady calculations were performed. For spatial discretization, the Roe scheme with 3rd order MUSCL and local time stepping with LU-SGS scheme were used. Calculations were carried out using both Baldwin-Lomax and Spalart-Allmaras turbulence models. No transition model has been utilized and flow has been considered as fully turbulent during the flow simulations for VFE-2. Different solutions are discussed in detail in the following sections.

28.1.2 Numerical Grid and Boundary Conditions

Single block grid which is provided by EADS-M was used for the flow simulations within this study and grid is illustrated in Figure 28-1. This grid is a C-Mesh around the apex of the wing and at the cross sections it is of O-type. The single block grid has been decomposed into 8 sub domains with point matching interfaces and used in parallel computations. It has dimensions of 128 x 160 x 96 in span wise, stream wise and boundary layer directions, respectively with a 2,092,872 number of total nodes. Multi-blocks were obtained by dividing the single block mesh in the axial direction. First three blocks enclose wall boundaries, only for the delta wing. The following blocks, numbered 4, 5 and 6, include wall boundaries for both wing and sting and the rest of the blocks include the sting. The multi-block structure is shown in Figure 28-2. All sub domains consist of almost similar dimensions for the sake of balancing the load on each processor. This results in increased efficiency of parallel simulation. The first cell height was chosen so that it has a y+ value between 0.2 and 3.7, an average of 1.5.

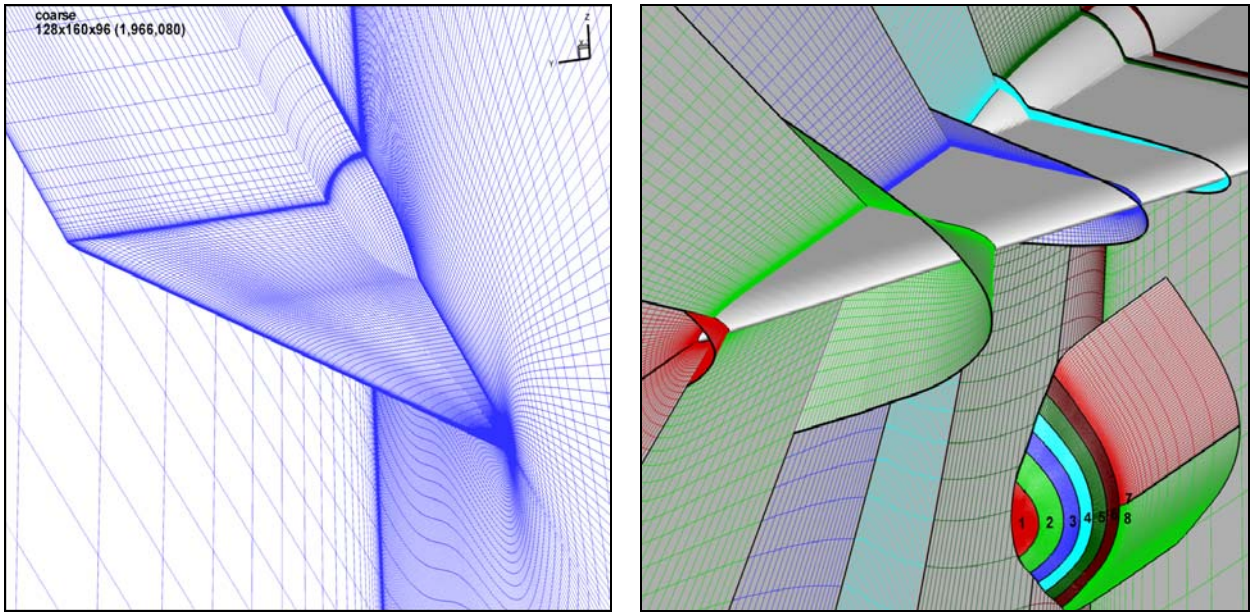

Figure 28-1: Computational Grid, Multi-Block Mesh Structure.

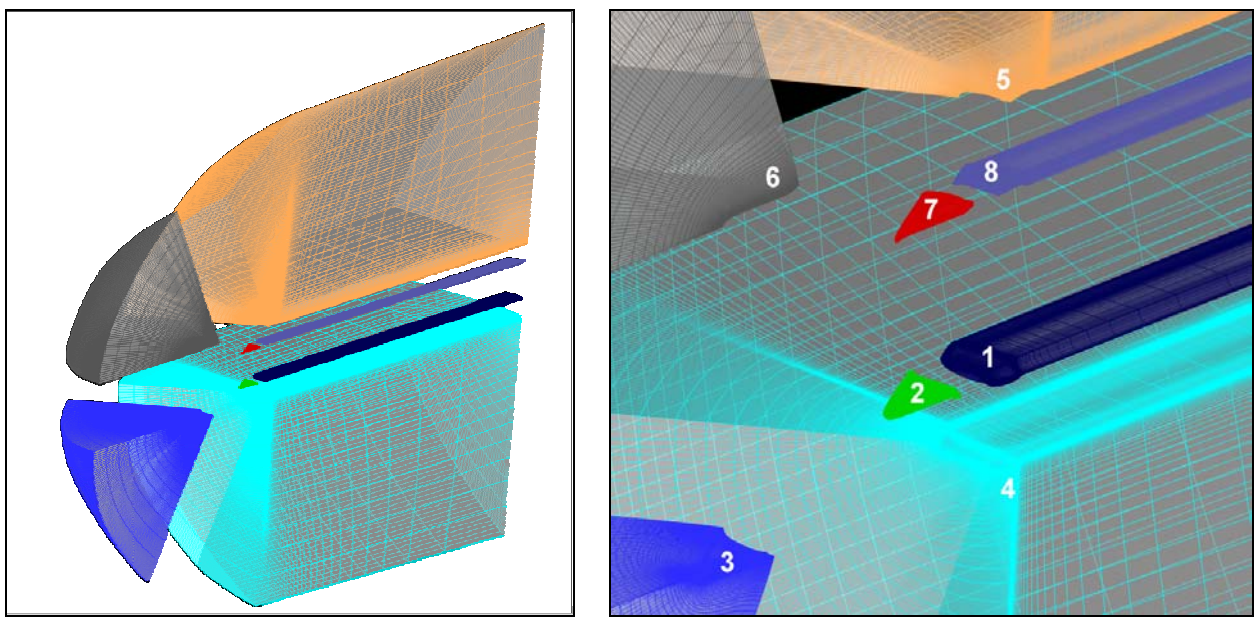

Figure 28-2: Close View of Sub Domains.

Half of the delta wing was modelled with a symmetry boundary condition. The boundary condition for the solid walls is adiabatic, no-slip type. Outer boundary was located nearly 7 chord lengths from the surface of the wing and 4 chord lengths away in the wingspan direction. At the outer boundary, far field boundary condition was applied.

28.2 TEST CASES

Table 28-1 shows the test matrix for the first computations, carried out by TAI. These calculations were performed with Baldwin Lomax turbulence model and they were used to evaluate the solver, xFLOWg. The wind tunnel test measurements of these cases were provided by Langley National Transonic Facility at NASA [[28-5], [28-6], [28-7], [28-8]]. For a constant Reynolds number of 6 million, subsonic and transonic cases were chosen. Angle of attack variation from 13.3 to 22.6 degree was also investigated for both medium radius and sharp leading edge types. Even though results for all cases were not mentioned, they were listed here for the sake of completeness.

Table 28-1: Test Cases, Analysed with Baldwin-Lomax Turbulence Model

Case	Geometry	Mach	AoA (deg.)	Reynolds (Mil.)
1	SHARP	0.851	13.5	6.0
2	SHARP	0.850	17.5	6.0
3	SHARP	0.851	18.6	6.0
4	SHARP	0.850	20.6	6.0
5	SHARP	0.850	22.6	6.0
6	SHARP	0.400	13.3	6.0
7	SHARP	0.401	17.4	6.0
8	SHARP	0.400	18.4	6.0
9	SHARP	0.401	20.5	6.0
10	SHARP	0.401	22.5	6.0
11	MEDIUM RAD.	0.400	13.3	6.0
12	MEDIUM RAD.	0.400	16.4	6.0
13	MEDIUM RAD.	0.400	18.4	6.0
14	MEDIUM RAD.	0.400	20.4	6.0
15	MEDIUM RAD.	0.400	22.4	6.0
16	MEDIUM RAD.	0.851	13.4	6.0
17	MEDIUM RAD.	0.849	16.5	6.0
18	MEDIUM RAD.	0.849	18.5	6.0
19	MEDIUM RAD.	0.850	20.6	6.0
20	MEDIUM RAD.	0.850	22.6	6.0

In the next stage, instead of Baldwin-Lomax, Spalart-Allmaras turbulence model was used. In order to evaluate the performance of these two turbulence models, 6 cases were studied which were listed in Table 28-5. Selected 6 cases were all at transonic speeds, 4 of them were from the cases listed in Table 1 and other two cases are at

higher angle of attack. The aim of calculations for these additional two cases was to evaluate the flow solver at high angle of attack cases since modelling the phenomenon at high angles of attack is challenging. Finally, focus was identification of the different flow regimes and confirmation of validity of the solver. It is aimed to see the compressibility effects, effect of the leading edge bluntness and angle of attack variation. The test cases studied were listed in the following tables (Table 28-2, Table 28-3, Table 28-4) and for convenience the VFE-2 test matrix nomenclature has been kept.

Table 28-2: Leading Edge Bluntness Effect

Case	Geometry	AoA(deg.)	Mach	Reynolds (Mil.)
11	SLE	18.5	0.2	2
12	RLE	18.5	0.2	2
26	SLE	23.0	0.85	6
27	RLE	23.0	0.85	6

Table 28-3: Angle of Attack Effect, RLE, Re = 6E+6

Case	AoA(deg.)	Mach
5	13.3	0.4
14	18.5	0.4
23	23.0	0.4

Table 28-4: Mach Number Effect, RLE, Re = 6E+6

Case	AoA(deg.)	Mach
23	23	0.4
26	23	0.85

28.3 RESULTS AND DISCUSSION

In this section, only representative cases were chosen to discuss the results of the study. Algebraic Baldwin-Lomax and one equation Spalart-Allmaras turbulence models were compared. Once the numerical concerns were fixed, physical phenomena became the focus of the study. For that goal, Mach number, angle of attack, and leading edge bluntness effects on the flow field were described in detail.

28.3.1 Flow Solver (xFLOWg) Evaluation

The first computations were carried out with algebraic Baldwin-Lomax turbulence model. This model is comparably straightforward, but it did not give acceptable results. Results of only Case 1 from the 20 test cases listed in Table 28-1, were explained here to draw conclusion. Computations for all other cases show similar behavior as Case 1.

As can be seen in Figure 28-3, pressure coefficient (C_p) distribution on the surface of the wing was shown for the sharp leading edge configuration. Mach number is 0.851 with an angle of attack 13.4 degree. Pressure coefficient variation at 5 chord wise locations were plotted and compared with the experimental data. Close to the leading edge, only average values were obtained. At x/c_r = 0.2 and 0.4 locations, suction peaks could not be resolved. This also resulted in inaccurate predictions at further downstream locations.

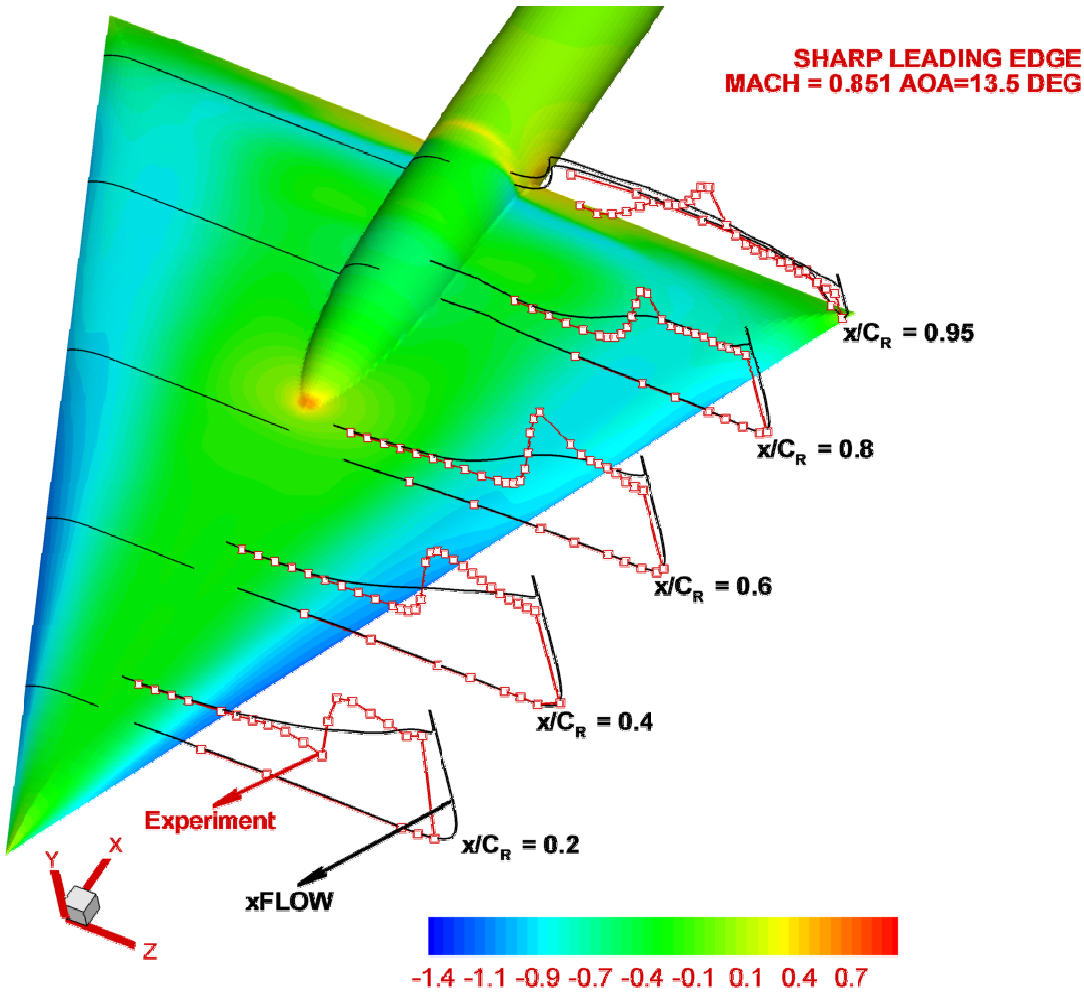

Figure 28-3: C_p Comparisons at x/c_r = 0.2, 0.4, 0.6, 0.8, 0.95 Chord Wise Locations and Surface C_p Plot (Case 1, Table 28-1).

Even though C_p is not totally in agreement with the experimental data, some of the characteristics of the vortical flow structure can be seen. To illustrate the flow patterns clearly, vorticity magnitude lines at different locations and stream lines are shown in Figure 28-4. Streamlines just from the apex rolls into the aft of the wing and forms the longitudinal vortex and flow separates at the leading edge of the wing.

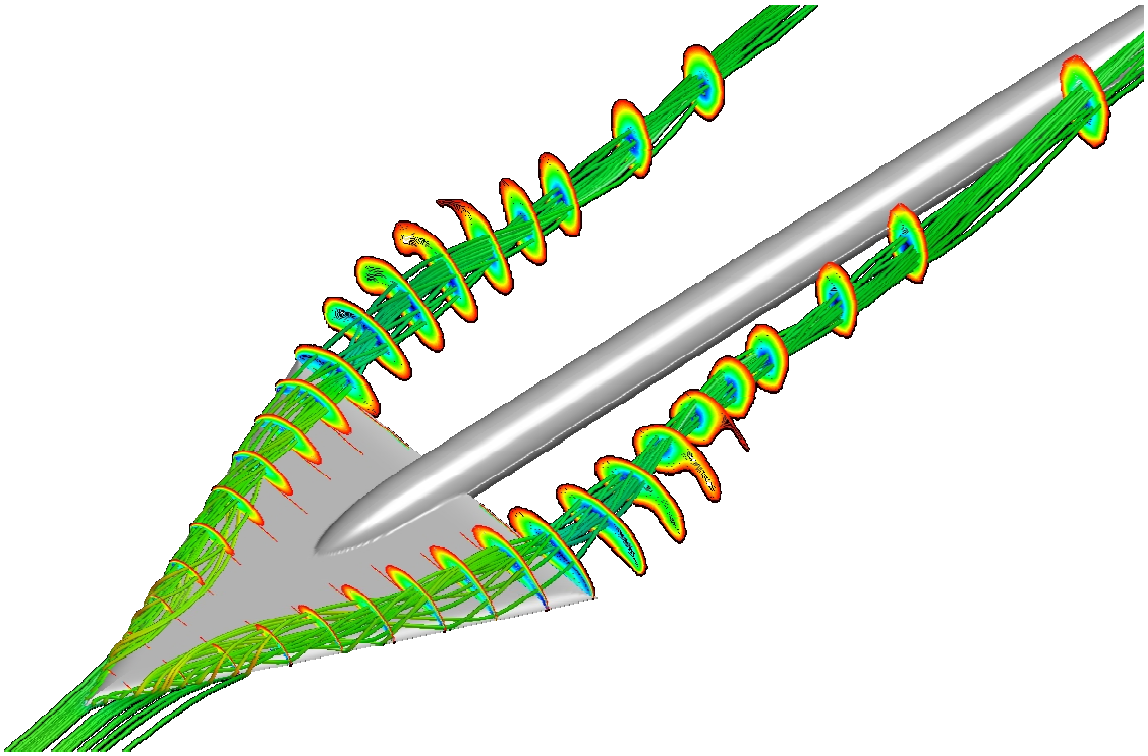

Figure 28-4: Vorticity Magnitude Contours and Stream Lines (Case 1, Table 28-1).

Also, normal force coefficients were calculated for comparison with the measurements. Figure 28-5 shows the normal force coefficient variation versus angle of attack for sharp leading edge configuration at both subsonic and transonic regimes. As can be seen, surprisingly normal force coefficients seem to be in better agreement. The reason for this situation can be understood by referring back to the Figure 28-3. It can be seen that close to apex region, at chord wise locations of 0.2 and 0.4 C_p distribution obtained is correct in the average sense. Since force is obtained by integrating the pressure, results are close to the measurements.

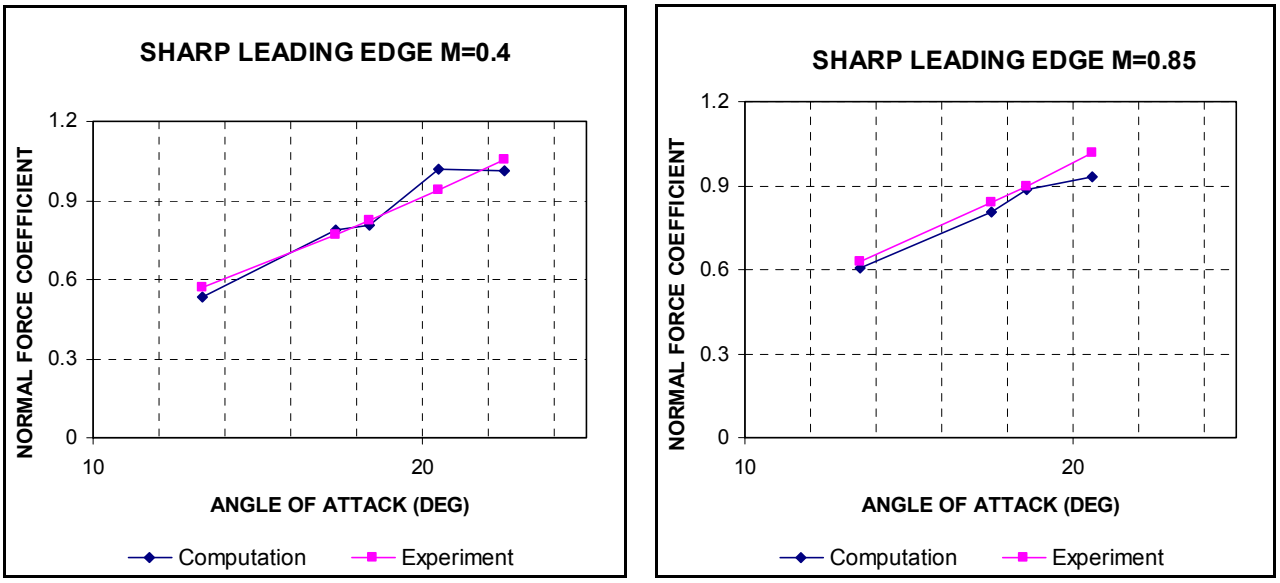

Figure 28-5: Comparison of Normal Force Coefficients for Sharp Leading Edge Configuration for 0.4 and 0.85 Mach Numbers.

For this specific case and for other cases, inaccurate C_p distribution is mainly due to miss prediction of the onset of separation, inaccurate resolution of vortex shock interaction and vortex breakdown or coupling of these depending on the case. It is difficult to draw reliable physical conclusions from such simulations. It seems that Baldwin-Lomax model does not simulate essential characteristics of this complex vortical flow field.

One of the drawbacks of Baldwin-Lomax turbulence model is that it yielded average values at the vortical regions. Suction peaks representative of the vortical regions could not be obtained properly. Turbulence model is important for resolving this type of vortex dominated flows. In the following sections of this study, instead of Baldwin-Lomax, Spalart-Allmaras turbulence model was used. Special attention was paid for 6 transonic test cases which are listed in Table 28-5. With these test cases, focus is on resolving shock-vortex interaction which turned out to be another challenge for the numerical simulations. Also, high angle of attack cases were chosen to capture vortex breakdown.

Table 28-5: Test Cases for Turbulence Model Study [28-5], [28-8]

Run No	Leading Edge	Point No	AoA (deg.)	Mach	Re (Mil.)
7	MRLE	141	13.4	0.851	6.0
7	MRLE	144	18.5	0.849	6.0
7	MRLE	147	24.6	0.850	6.0
88	SLE	1945	13.5	0.851	6.0
88	SLE	1950	18.6	0.851	6.0
88	SLE	1956	24.6	0.851	6.0

Presence of the longitudinal vortex can be observed with Spalart-Allmaras turbulence model compared to Baldwin-Lomax turbulence model [Figure 28-6]. Streamlines above the surface separate in the front region and rolls into a vortex as can be seen in Figure 28-7. The suction peaks on the upper surface of the wing were captured for "Run No 7" at an angle of attack 18.5 degrees. However, especially close to the apex the strength of the so called primary vortex could not be predicted fairly and the second peaks observed in the experiments were not resolved in the calculations. The presence of those secondary inner vortices is highly dependent on the correct prediction of the strength and location of the primary vortex [28-9]. Beside turbulence model concern, relatively coarse grid might be one reason for not resolving this inner vortex.

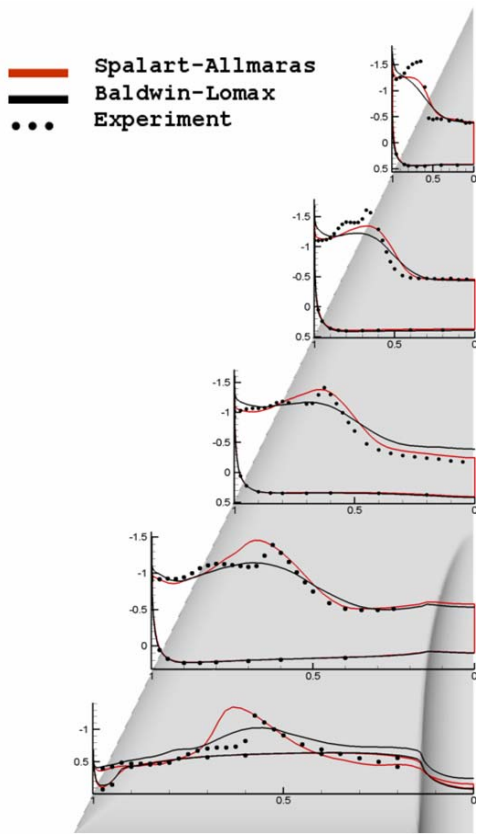

Figure 28-6: C_p Comparisons at x/c_r = 0.2, 0.4, 0.6, 0.8, 0.95 Chord Wise Locations (Point No 144, Table 28-5).

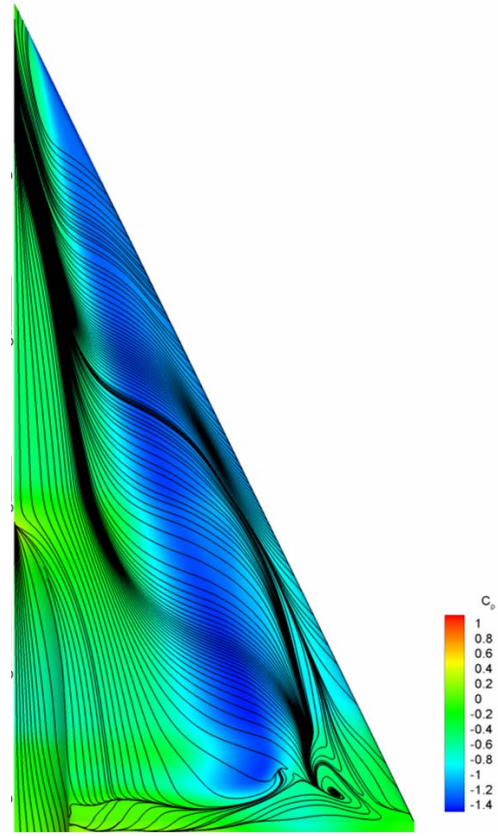

Figure 28-7: Streamlines Close to the Surface on the Suction Side of the Wing (Point No 144, Table 28-5).

At higher angle of attack, 24.6 degree experiment shows the vortex breakdown phenomenon at the rear part of the wing whereas this feature was not captured in the calculations. However, close to the apex separated flow without vortex breakdown was captured successfully (Figure 28-8).

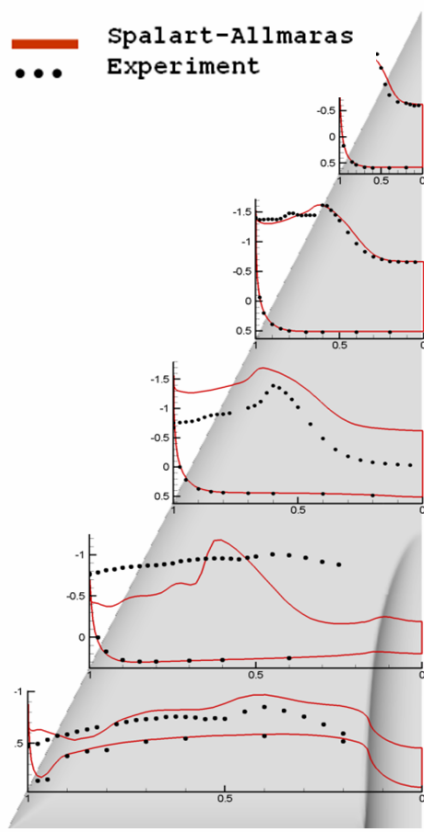

Figure 28-8: C_p Comparisons at x/c_r = 0.2, 0.4, 0.6, 0.8, 0.95 Chord Wise Locations (Point No 147, Table 28-5).

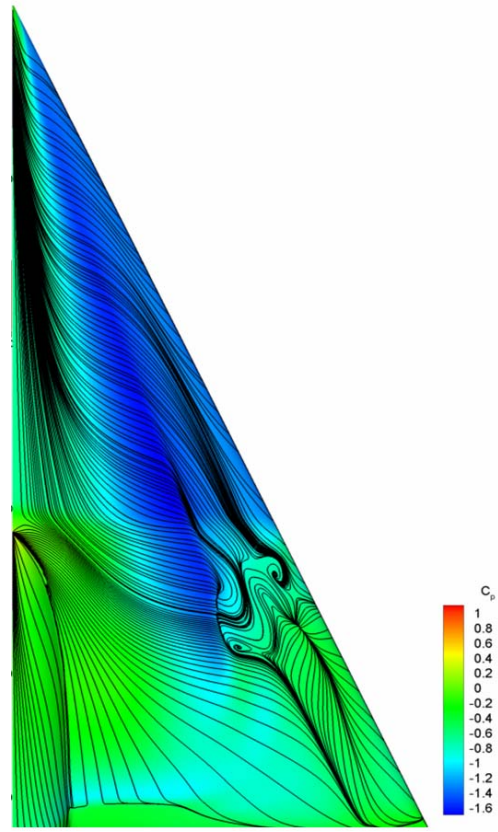

Figure 28-9: Streamlines Close to the Surface on the Suction Side of the Wing (Point No 147, Table 28-5).

There is also some discrepancy with the experimental data as plotted in Figure 28-10, for the sharp leading edge configuration. Vortical flow in the front part of the wing could not be predicted reasonably. On the other hand, Spalart-Allmaras turbulence model produces proper results compared to Baldwin Lomax turbulence model. Especially close to the trailing edge, vortex strength and location predictions are in better agreement with the measurements.

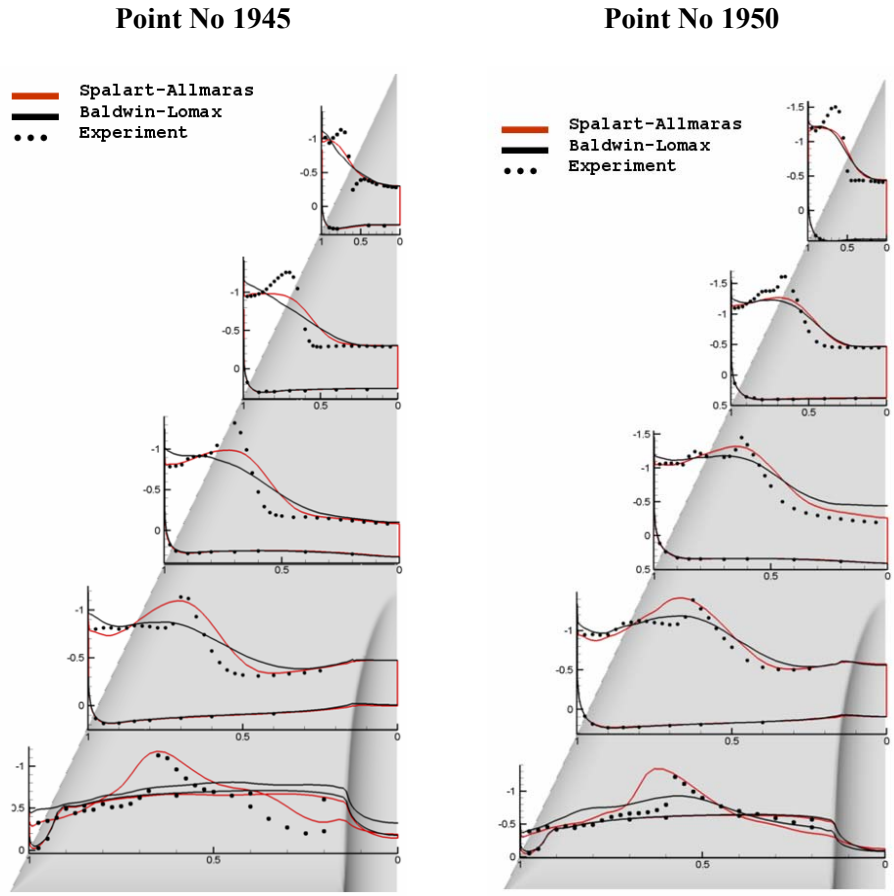

Figure 28-10: C_p Comparisons at x/c_r = 0.2, 0.4, 0.6, 0.8, 0.95 Chord Wise Locations (Point No 1945, 1950, Table 28-5).

The above figures (Figure 28-6, Figure 28-8, Figure 28-10) show that prediction capability of the solver was significantly improved with implemented Spalart-Allmaras turbulence model. In the rest of the study, focus is on the detailed description of the flow field. Angle of attack, compressibility and leading edge bluntness effects on the flow field characteristics were presented. As will be clear in the following section, flow characteristics are strongly dependent on the above stated items, and clear distinction can be made on the governed flow physics. First emphasis is on the validation of the test cases before explaining the physics behind.

28.3.2 Comparison with Experimental Results

Following figures show the pressure coefficient comparison between the experimental and computational results of the cases studied. The solid lines correspond to numerical results and the dots represent the measured values. Numerical results mostly match well with the experimental data at subsonic and transonic speeds for sharp and round leading edge configurations. As shown in Figure 28-11 and Figure 28-19, the suction peaks and their locations were predicted well at chord wise and span wise locations. There is a discrepancy between numerical and experimental values close to apex for Case 11 and 12 as can be seen in Figure 28-11. The suction peak corresponding to strength of primary vortex was under predicted. However, further downstream flow development was correctly simulated and solutions matched with the experimental data satisfactorily.

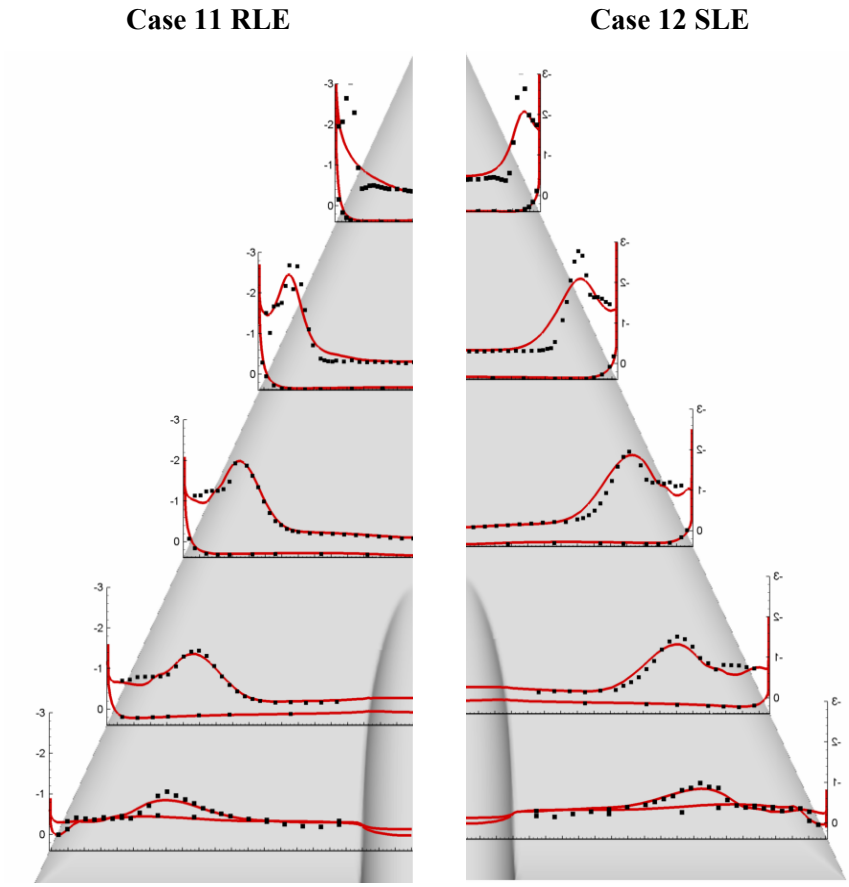

Figure 28-11: C_p Comparisons at x/c_r = 0.2, 0.4, 0.6, 0.8, 0.95 Chord Wise Locations (Case 11-12, Table 28-2).

Vortical flow structure was resolved well for Case 26 and 27 even at the upstream locations compared to Case 11 and 12. In fact, flows in Case 11 and 12 are incompressible. Since xFLOWg is a compressible solver, there is a need of a prediction method for incompressible flows. Though, satisfactory results for compressible cases confirm the validity of the solver.

Case 26 RLE **Case 27 SLE**

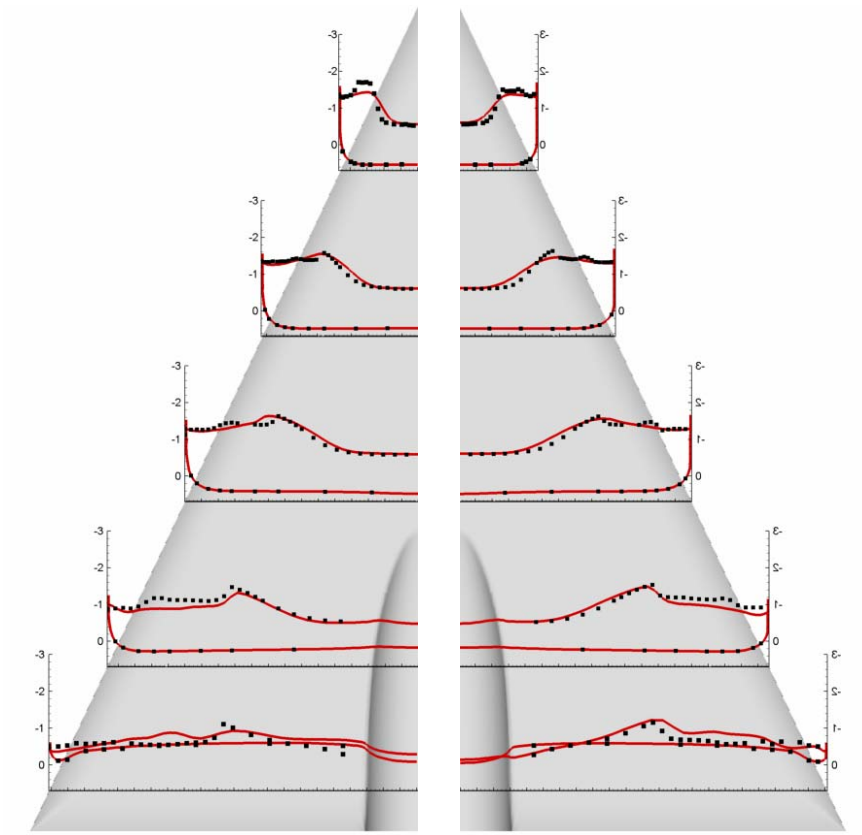

Figure 28-12: C_p Comparisons at x/c_r = 0.2, 0.4, 0.6, 0.8, 0.95 Chord Wise Locations, (Case 26-27, Table 28-2).

Figure 28-13 shows that there is a slight disagreement at the highest angle of attack, but again topology of the vortical flow field was resolved well. At high angles of attack, unsteadiness of flow dominates the problem. In this study all the calculations were done at steady state conditions. As a result, solution for this case might be improved by taking unsteadiness into account. Also, better resolution of the grid or solution based grid adaptation might yield better results.

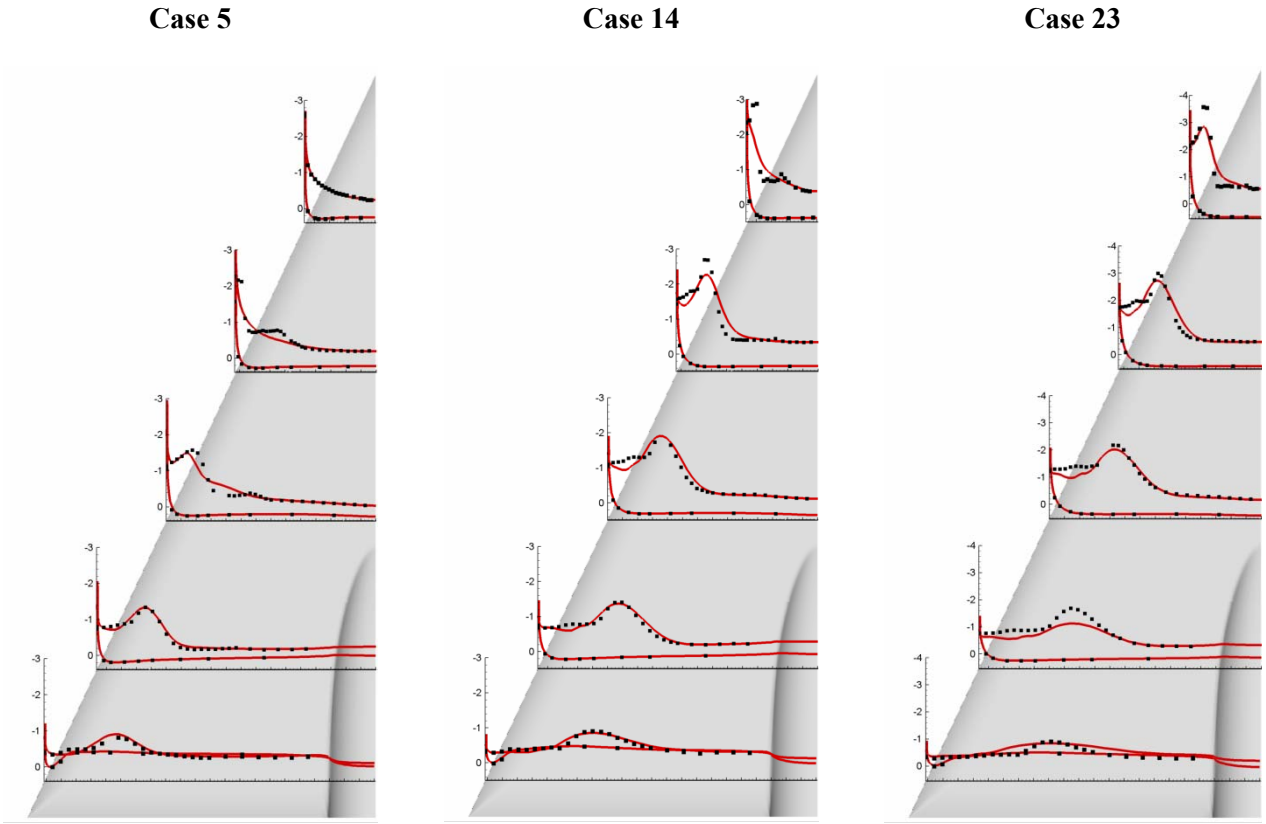

Figure 28-13: C_p Comparisons at x/c_r = 0.2, 0.4, 0.6, 0.8, 0.95 Chord Wise Locations (Case 5 ,14, 23, Table 28-3).

28.3.3 Some Factors Influencing the Vortical Flow Field

Following sections were dedicated for better understanding of the physical aspects of the flow field for a range of Mach number, and angles of attack. It is seen that features of flow is highly dependent on these parameters. Also, depending on the shape of the leading edge different flow features were observed.

28.3.3.1 Influence of Mach Number

Case 23 and 26 with Mach number of 0.4 and 0.85 for medium radius leading edge configuration were selected to investigate the compressibility effect on the flow field. Angle of attack is 23 degree, and vortex breakdown phenomenon is also present. As illustrated in Figure 28-14, Figure 28-15, Figure 28-16**,** Figure 28-17, increase in Mach number results in:

- Movement of primary vortex to the inboard;
- Increase in vortex strength;
- Stronger secondary vortex formed close to leading edge;
- Decrease in suction peak in the surface pressure distribution; and
- Onset of separation closer to the apex.

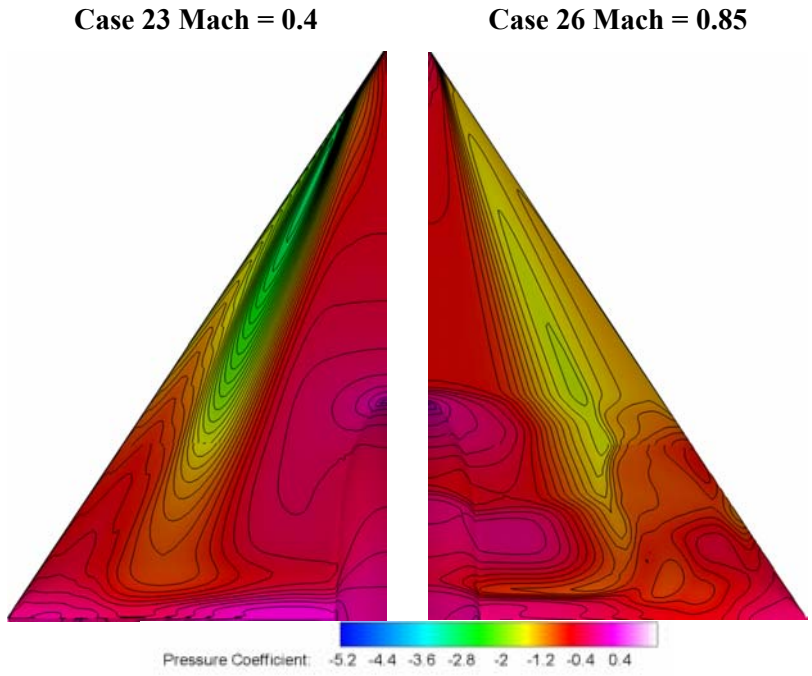

Figure 28-14: Surface Pressure Contours (Case 23 and 26, Table 28-4).

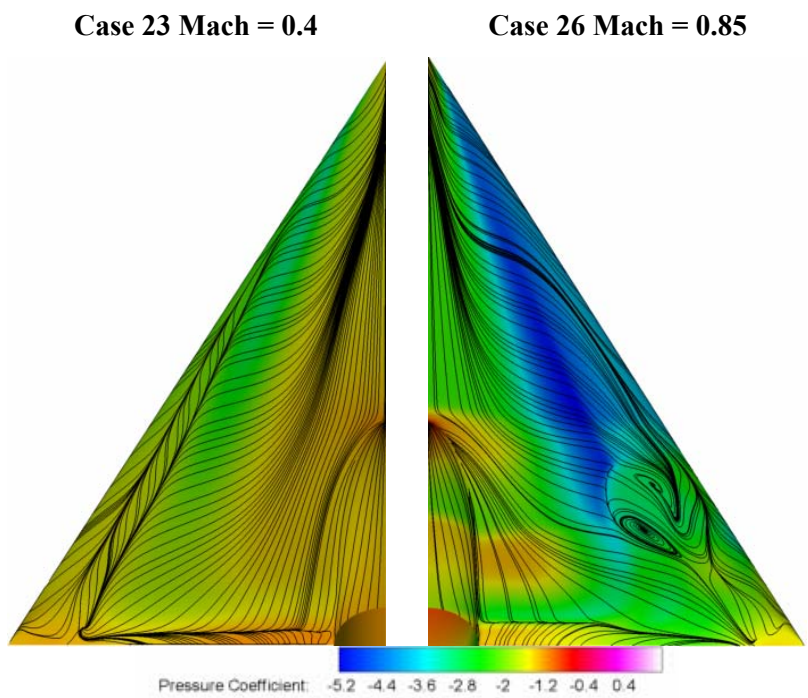

Figure 28-15: Streamlines Close to the Surface (Case 23 and 26, Table 28-4).

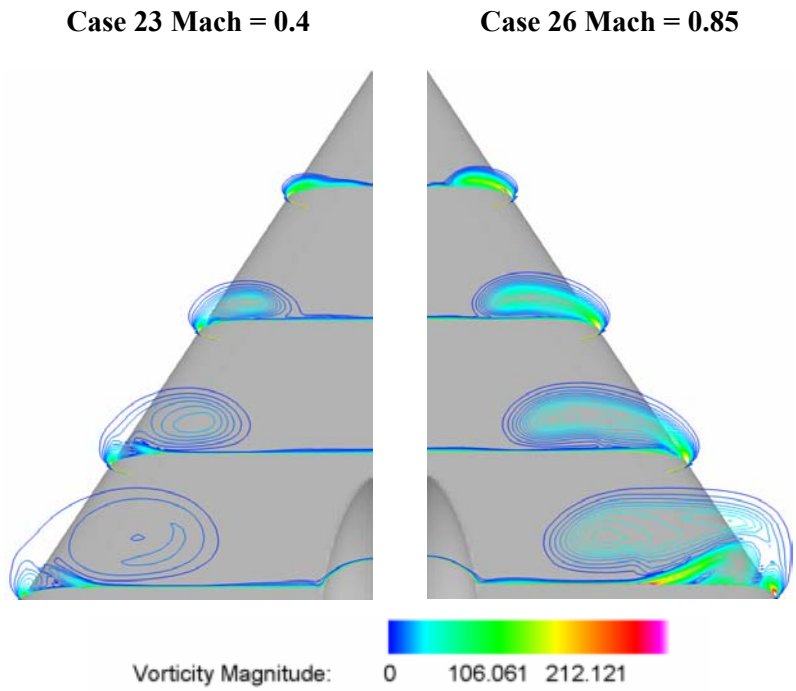

Figure 28-16: Vorticity Magnitude Isolines at Various Chord Wise Locations (Case 23 and 26, Table 28-4).

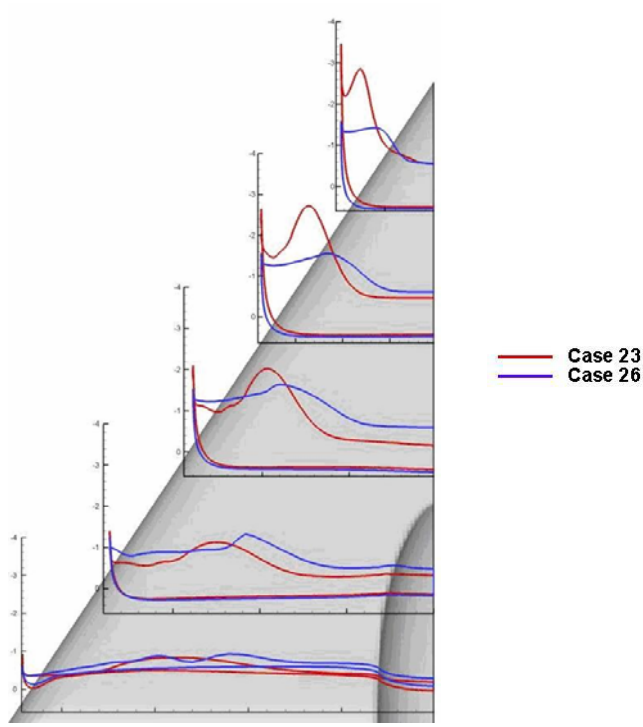

Figure 28-17: C_p Lines at x/c_r = 0.2, 0.4, 0.6, 0.8, 0.95 Chord Wise Locations (Case 23 and 26, Table 28-4).

A shock is observed for Case 26, on the delta wing close to the nose of the sting, and two other cross shocks were also seen close to the rear part of the wing as shown in the Figure 28-15. This case was challenging since interaction between vortex and the shocks were not easy to describe. Resolving this feature resulted in accurate C_p distribution on the surface of the wing.

28.3.3.2 Influence of Leading Edge Bluntness

Rounded leading edge (RLE) and sharp leading edge (SLE) configurations have similar basic flow patterns. The difference for RLE is that, primary separation line is no longer at leading edge. The leading edge curvature is one of the parameters influencing the onset of flow separation. Flow separates just from the apex of the leading edge for SLE while for RLE there is a larger area of attached flow around the apex at low angle of attack as shown in the Figure 28-19. Comparing the Case 11 and 12, with a Mach number of 0.2 and 18.5 degree angle of attack, the main difference is at the fore part of the wing. For high angle of attack and high speed flow condition, vortical core moves slightly toward inboard for the sharp leading edge (Case 26 and 27). The two cases show that bluntness has a significant influence on the flow field at low angle of attacks and low Mach numbers but when the flow conditions are vigorous, flow features over delta wing is less affected by leading edge type.

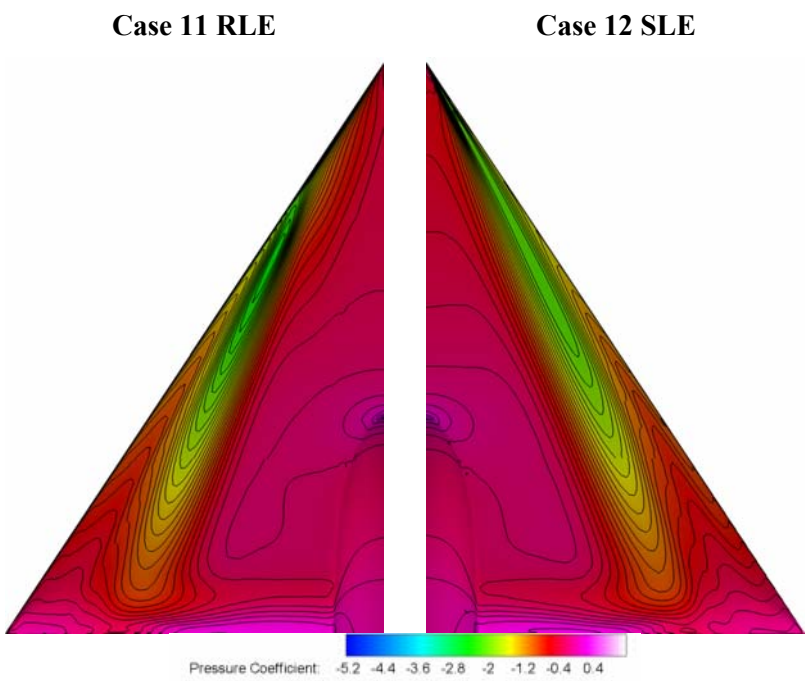

Figure 28-18: Surface Pressure Contours (Case 11 and 12, Table 28-2).

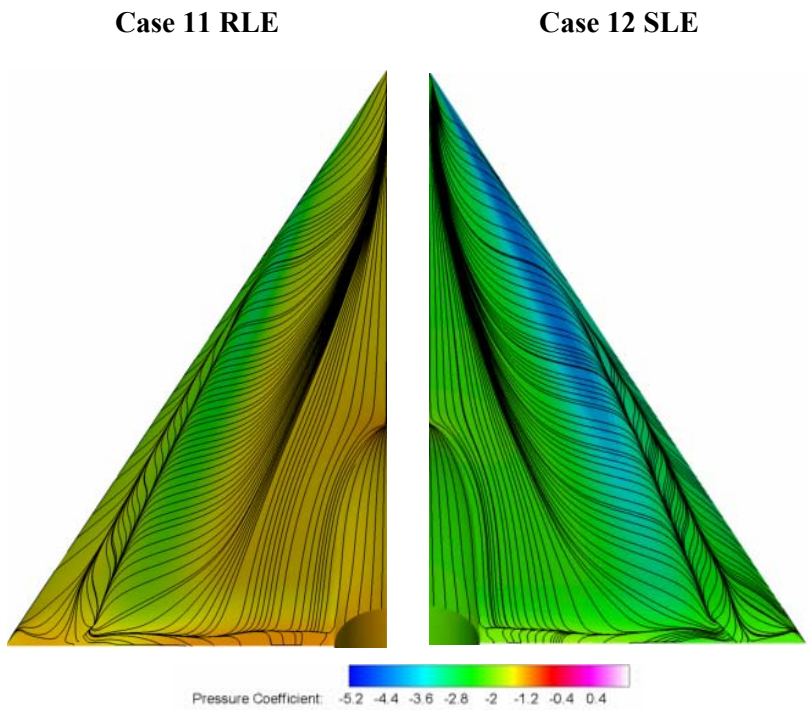

Figure 28-19: Streamlines Close to the Surface (Case 11 and 12, Table 28-2).

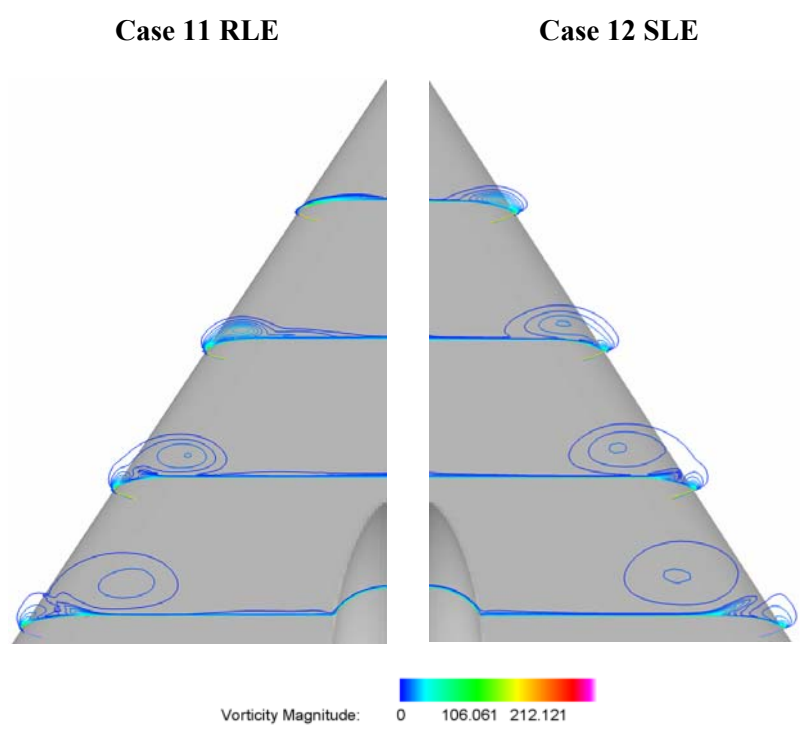

Figure 28-20: Vorticity Magnitude Isolines at Various Chord Wise Locations (Case 11 and 12, Table 28-2).

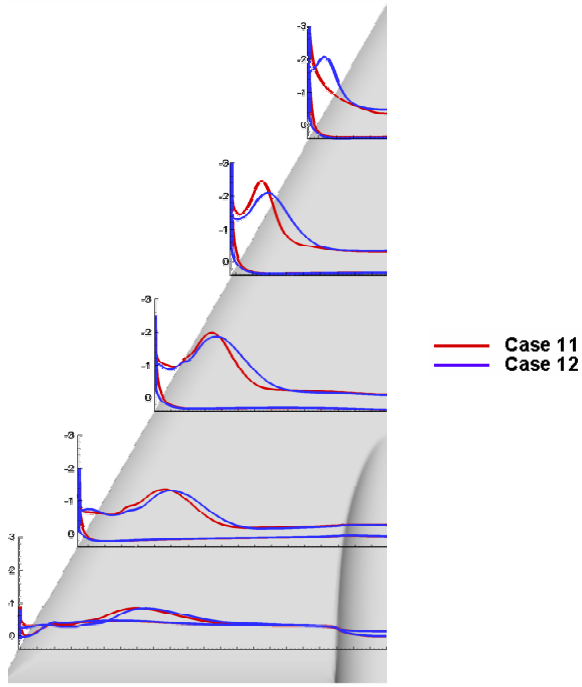

Figure 28-21: C_p Lines at x/c_r = 0.2, 0.4, 0.6, 0.8, 0.95 Chord Wise Locations (Case 11 and 12, Table 28-2).

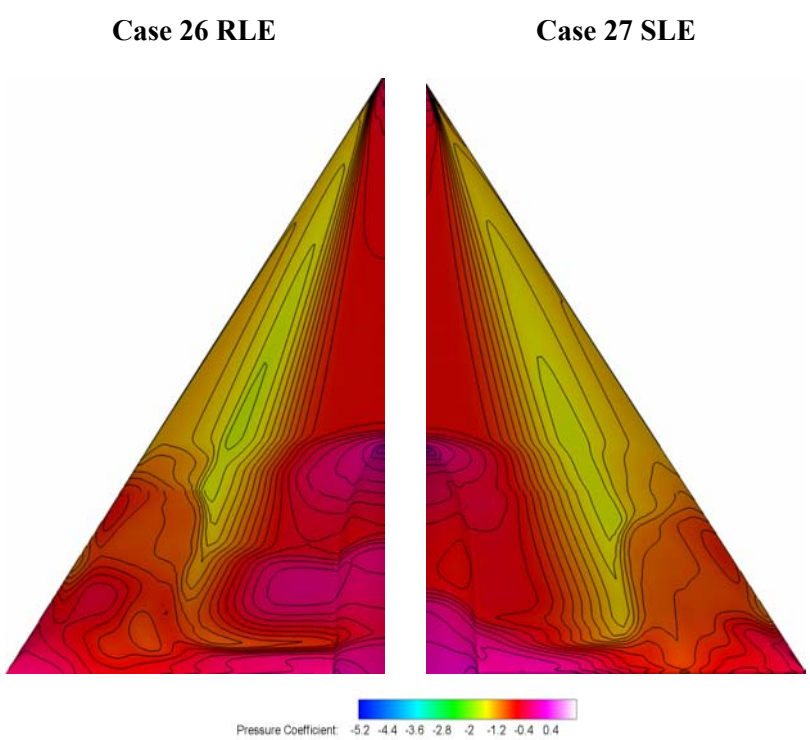

Figure 28-22: Surface Pressure Contours (Case 26 and 27, Table 28-2).

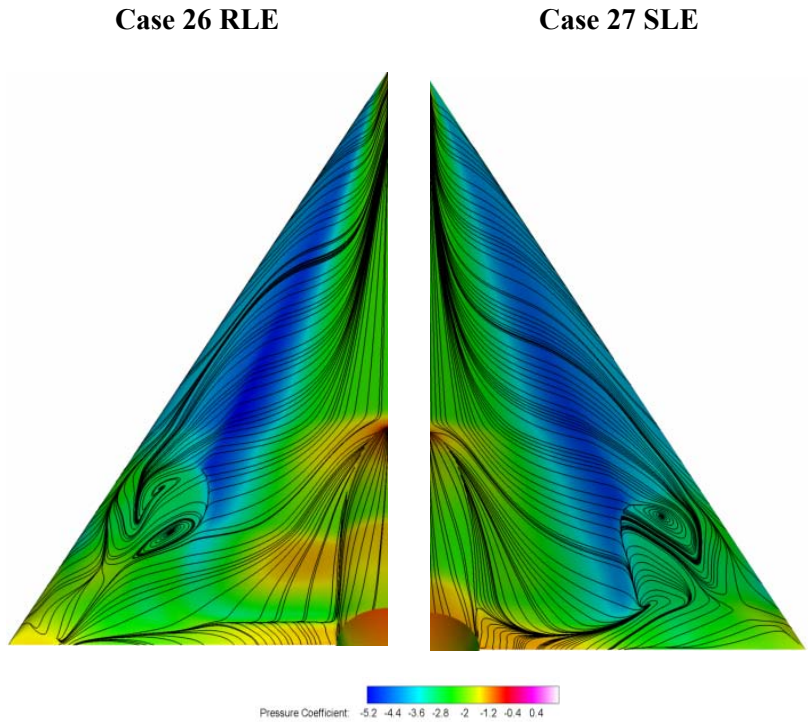

Figure 28-23: Streamlines Close to the Surface (Case 26 and 27, Table 28-2).

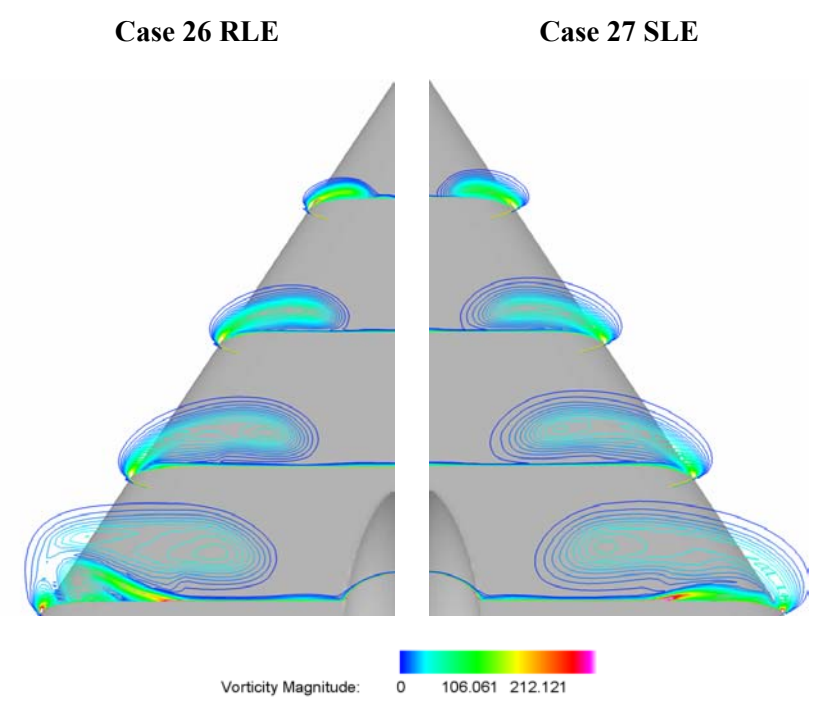

Figure 28-24: Vorticity Magnitude Isolines at Various Chord Wise Locations (Case 26 and 27, Table 28-2).

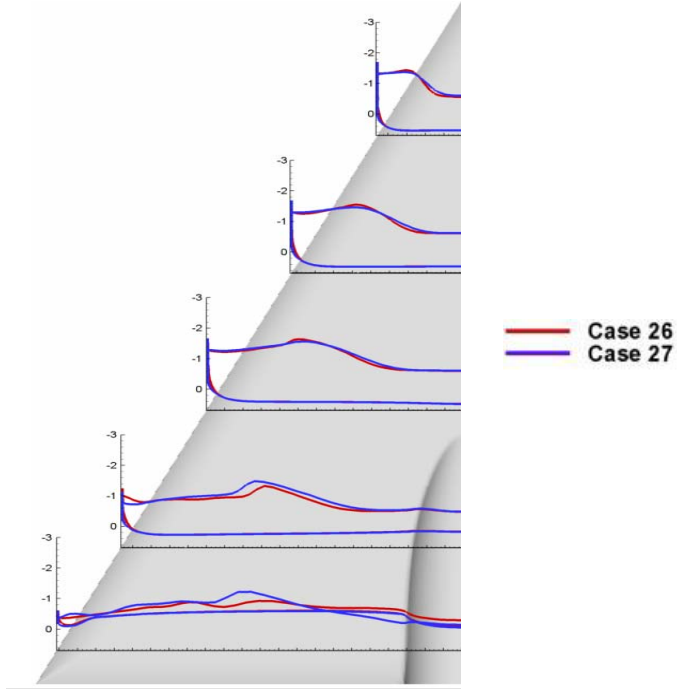

Figure 28-25: C_p Lines at x/c_r = 0.2, 0.4, 0.6, 0.8, 0.95 Chord Wise Locations (Case 26 and 27, Table 28-2).

28.3.3.3 Influence of Angle of Attack

To investigate the angle of attack effect, Case 5, Case 14 and Case 23 were compared. All cases are for rounded leading edge configuration with a Mach number of 0.85 and Reynolds number of 6 million. Figure 28-26 and Figure 28-27 show the C_p distribution on the upper surface of the wing. Streamlines and vorticity magnitude lines at three different angles of attack were drawn in the following figures.

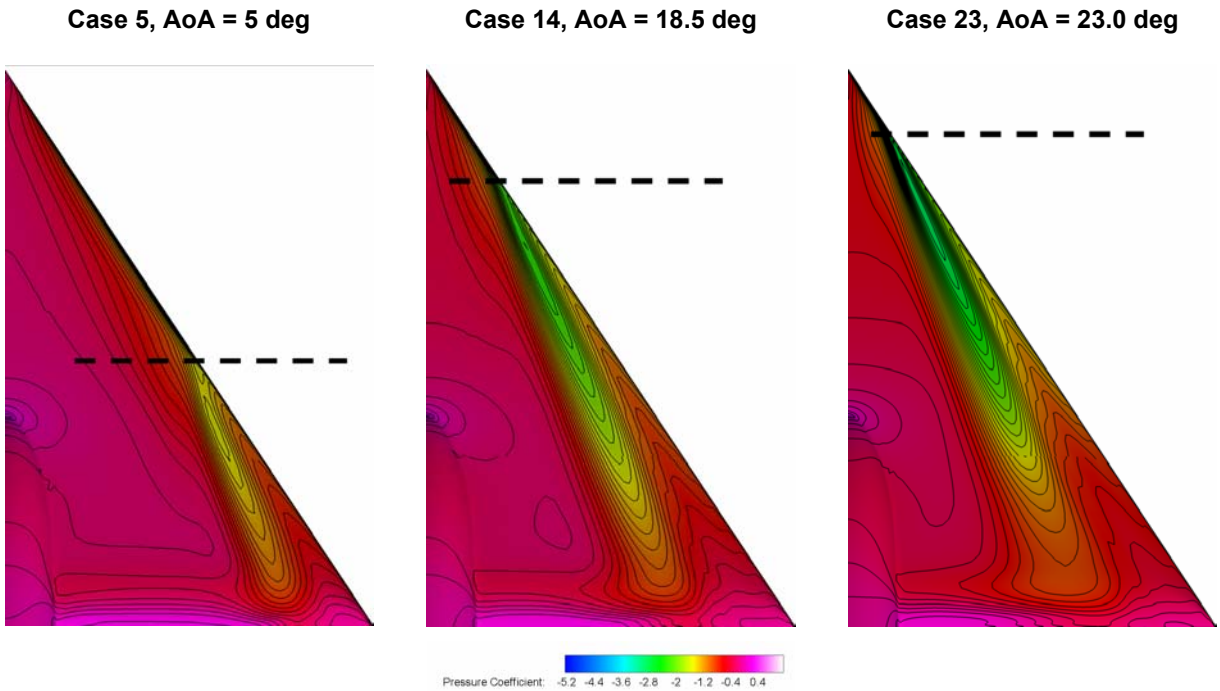

Figure 28-26: Surface Pressure Contours (Case 5, 14 and 23, Table 28-3).

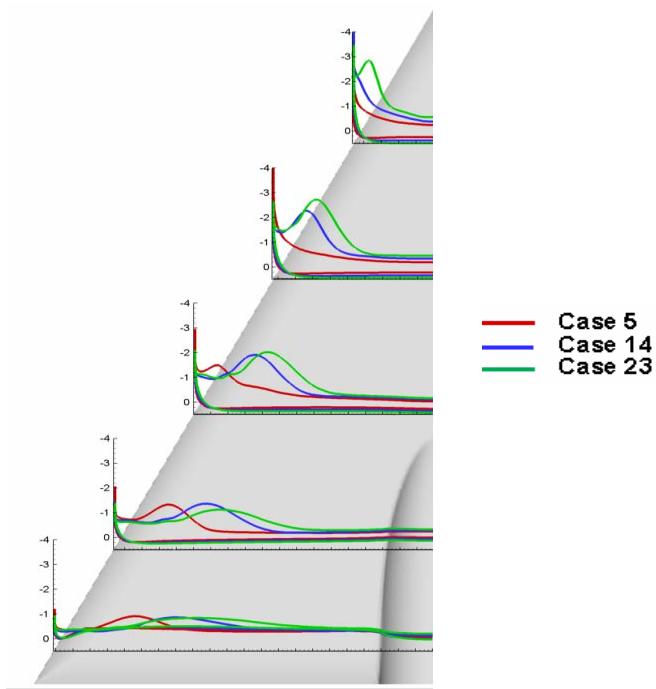

Figure 28-27: C_p Lines at x/c_r = 0.2, 0.4, 0.6, 0.8, 0.95 Chord Wise Locations (Case 5, 14 and 23, Table 28-3).

For case 5, it is clearly seen that flow is mostly attached on the surface as can be seen from the Figure 28-26 and Figure 28-28. The onset of the leading edge vortex is close to $x/c_r = 0.5$ location as shown in Figure 28-26. Case 14 is again for the round leading edge configuration at higher angle of attack, the leading edge separation moves towards to the apex as shown in Figure 28-26. As shown in Figure 28-29, Figure 28-31, and Figure 28-33, vortex strength increases with the angle of attack, attachment and separation lines are also obvious in Figure 28-28, Figure 28-30, Figure 28-32 for the three angles of attack.

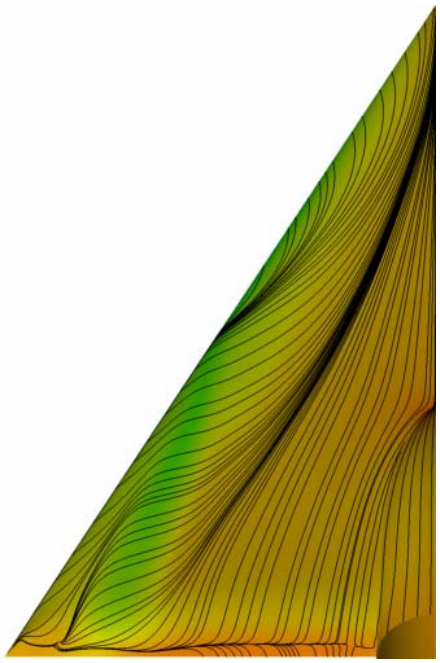

Figure 28-28: Streamlines Close to the Surface (Case 5, Table 28-3).

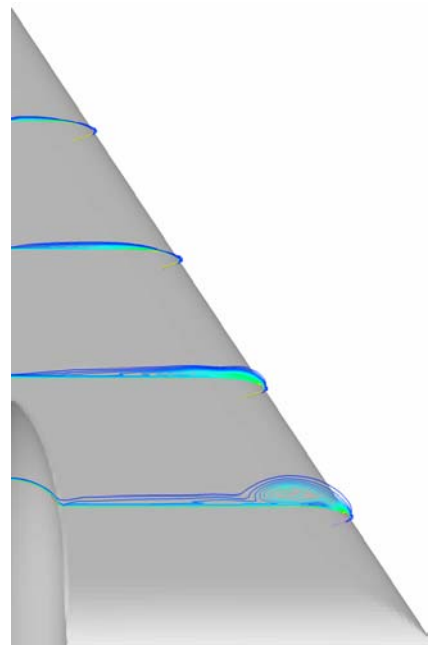

Figure 28-29: Vorticity Magnitude Isolines at Various Chord Wise Locations (Case 5, Table 28-2).

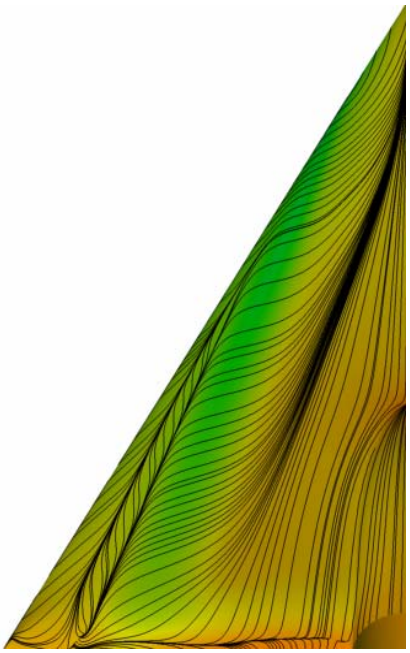

Figure 28-30: Streamlines Close to the Surface (Case 14, Table 28-3).

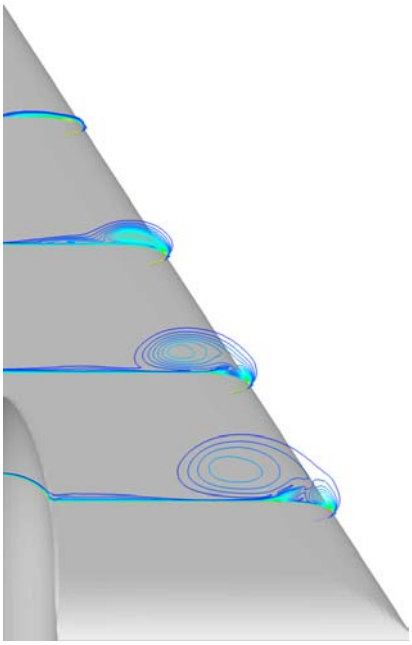

Figure 28-31: Vorticity Magnitude Isolines at Various Chord Wise Locations (Case 14, Table 28-2).

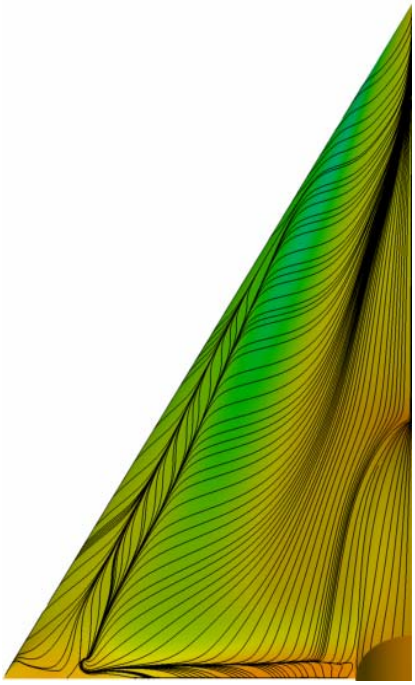

Figure 28-32: Streamlines Close to the Surface (Case 23, Table 28-3).

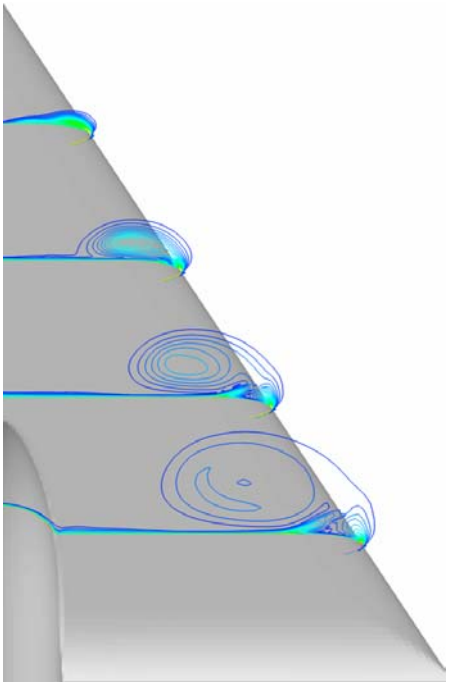

Figure 28-33: Vorticity Magnitude Isolines at Various Chord Wise Locations (Case 23, Table 28-2).

In summary, increase in angle of attack results in:

- Onset of separation point movement toward the upstream;
- Higher vortex strength; and
- Vortex moving away from the leading edge towards to the center of the wing.

28.4 CONCLUSIONS

Within the framework of VFE-2 AVT-113 task group, TAI performed numerical calculations to investigate the vortical flow field characteristics on delta wing configuration. In-house developed structured, 3D Navier-Stokes solver has been used. Both subsonic and transonic cases with sharp and rounded leading edge configurations were numerically simulated. A range of angle of attack was chosen to investigate its effect on the flow field.

Two different turbulence models were used. Compared to Baldwin-Lomax, Spalart-Allmaras turbulence model resolved the vortical structure more properly. Significant improvement has been achieved on the predictions just by this turbulence model concern. It is concluded that the in-house developed solver yields reasonable results especially for the compressible flows. Discrepancies with the experimental data in incompressible regime were present. Therefore, to improve the solver capability for incompressible flows is under consideration. Another concern is that at high angle of attacks flow becomes unsteady. Since steady calculations result in some discrepancy with the experimental data, it is better to perform unsteady calculations for high angle of attack cases. In addition to these concerns, grid resolution is another important parameter on the results. Solution based grid adaptation will yield better results to resolve vortical and shock dominated flows.

Computations shed light on the physics of the flow field. From the physical point of view, effect of Mach number, leading edge bluntness, and angle of attack on the flow features of delta wings were investigated. Regarding the factor of leading edge bluntness, it is shown that as flow becomes vigorous, which means at high angles of attack and high speeds, leading edge type has less influence on the flow structure. Different flow phenomena govern the flow field depending on the angle of attack and classification can be done accordingly. Compressibility has also big importance on the vortical flow topology.

Both numerical and experimental studies gave better insight on the flow physics of delta wings. The studies made within this work group have led the evaluation of the CFD solvers of various participants. Comparison with both experiments and with other codes turned out to be beneficial for understanding and simulation of complex flow problems. Considerable improvement concerning the mentioned aspects has been achieved through the VFE-2 International Vortex Flow Experiment.

28.5 REFERENCES

[28-1] Gürdamar, E., Tarhan, E., Ortakaya, Y. and Korkem, B.: *Parallel Navier-Stokes Solutions of NASA 65° Delta Wing,* International Conference on Parallel Computational Fluid Dynamics, 21-24.05.2007 Antalya, Turkey.

[28-2] Tarhan, E., Ortakaya, Y., Gürdamar, E. and Korkem, B.: *Parallel Navier-Stokes Solutions of a Wing-Flap Configuration on Structured Multiblock Oversetting Grids*, International Conference on Parallel Computational Fluid Dynamics, 21-24.05.2007 Antalya, Turkey.

[28-3] Şahin, P., Gürdamar, E., Tarhan, E., Ortakaya, Y. and Korkem, B.: *Parallel Turbulent Navier-Stokes Solutions of Wing Alone Geometries Used in the Drag Prediction Workshop III*, International Conference on Parallel Computational Fluid Dynamics, 21-24.05.2007 Antalya, Turkey.

[28-4] Güzel, G., Ortakaya, Y. and Korkem, B.: *An Implementation and Validation Study on the Actuator Disk Model*, International Forum on Rotorcraft Multidisciplinary Technology, October 15-17, 2007 Seoul, Korea.

[28-5] Chu, J. and Luckring, J.M.: *Experimental Surface Pressure Data Obtained on 65° Delta Wing Across Reynolds Number and Mach Number Ranges, Volume 1 – Sharp Leading Edge, Appendix C*, NASA Technical Memorandum 4645, February 1996.

[28-6] Chu, J. and Luckring, J.M.: *Experimental Surface Pressure Data Obtained on 65° Delta Wing Across Reynolds Number and Mach Number Ranges, Volume 1 – Sharp Leading Edge, Appendix D*, NASA Technical Memorandum 4645, February 1996.

[28-7] Chu, J. and Luckring, J.M.: *Experimental Surface Pressure Data Obtained on 65° Delta Wing Across Reynolds Number and Mach Number Ranges, Volume 3 – Medium Radius Leading Edge, Appendix C*, NASA Technical Memorandum 4645, February 1996.

[28-8] Chu, J. and Luckring, J.M.: *Experimental Surface Pressure Data Obtained on 65° Delta Wing Across Reynolds Number and Mach Number Ranges, Volume 3 – Medium Radius Leading Edge, Appendix E*, NASA Technical Memorandum 4645, February 1996.

[28-9] Fritz, W. and Cummings, R.M.: *What was Learned from the Numerical Simulations for the VFE-2*, AIAA 2008-389, 46th AIAA Aerospace Sciences Meeting and Exhibit, 7-10 January 2008, Reno, Nevada.